Smartphone-based particle tracking velocimetry for the in vitro assessment of coronary flows

Medical Engineering and Physics 126 (2024) 104144

Contents lists available at ScienceDirect

Medical Engineering and Physics

journal homepage: www.elsevier.com/locate/medengphy

Paper

Smartphone-based particle tracking velocimetry for the *in vitro* assessment of coronary flows

Elena Torta [a], Bianca Griffo [a], Giuseppe C.A. Caridi [b], Giuseppe De Nisco [a], Claudio Chiastra [a], Umberto Morbiducci [a], Diego Gallo [a,*]

[a] Polito[BIO]Med Lab, Department of Mechanical and Aerospace Engineering, Politecnico di Torino, Turin, Italy
[b] Institute of Fluid Mechanics and Heat Transfer, TU Wien, Vienna, Austria

ARTICLE INFO

Keywords:
Particle tracking velocimetry
Particle image velocimetry
Coronary arteries
Smartphone
Low-power laser

ABSTRACT

The present study adopts a smartphone-based approach for the experimental characterization of coronary flows. Technically, Particle Tracking Velocimetry (PTV) measurements were performed using a smartphone camera and a low-power continuous wave laser in realistic healthy and stenosed phantoms of left anterior descending artery with inflow Reynolds numbers approximately ranging from 20 to 200. A Lagrangian–Eulerian mapping was performed to convert Lagrangian PTV velocity data to a Eulerian grid. Eulerian velocity and vorticity data obtained from smartphone-based PTV measurements were compared with Particle Image Velocimetry (PIV) measurements performed with a smartphone-based setup and with a conventional setup based on a high-power double-pulsed laser and a CMOS camera.

Smartphone-based PTV and PIV velocity flow fields substantially agreed with conventional PIV measurements, with the former characterized by lower average percentage differences than the latter. Discrepancies emerged at high flow regimes, especially at the stenosis throat, due to particle image blur generated by smartphone camera shutter speed and image acquisition frequency. In conclusion, the present findings demonstrate the feasibility of PTV measurements using a smartphone camera and a low-power light source for the *in vitro* characterization of cardiovascular flows for research, industrial and educational purposes, with advantages in terms of costs, safety and usability.

1. Introduction

The analysis of blood flow dynamics is crucial to understand vascular pathophysiology, to plan individualized treatment strategies, to design cardiovascular implantable devices and to optimize their performance [1–3]. In this context, the experimental characterization of the fluid dynamics in realistic cardiovascular phantoms becomes particularly relevant. State-of-the-art experimental fluid mechanics techniques applied to study cardiovascular flows include Particle Image Velocimetry (PIV) and Particle Tracking Velocimetry (PTV). PIV and PTV have been applied to perform quantitative analyses of the fluid dynamics within realistic cardiovascular models of healthy or diseased vessels [4–7], also in presence of blood recirculating devices such as left ventricular assist devices [8] and intravascular stents or prosthetic heart valves [9–16]. The main difference between the two experimental approaches is that PIV measures the mean displacement of a cluster of seeding particles within an interrogation area, whereas PTV tracks the motion of individual particles in the illuminated region. Based on this difference, hereafter we will refer to the specification of the flow field obtained from PIV or PTV as Eulerian or Lagrangian, respectively. Technically, PIV usually requires a homogeneous and relatively dense distribution of seeding particles, while PTV is less sensitive than PIV to non-uniform or low seeding particle densities [17], resolving local fluid motion more accurately [18]. This is a relevant advantage in flow separation or recirculation regions, where the local fluid dynamic conditions usually entail a low particle image density [18]. Moreover, PTV can achieve better spatial resolution and precision than PIV in near-wall regions [18,19], where PIV measurements may present bias errors due to the discretization in interrogation windows and the consequent averaging of particle displacements in presence of strong velocity gradients [19]. In addition, the Lagrangian representation of the flow obtained through PTV measurements enables the quantification of local residence times, highlighting the presence and extent of stagnation and

* Corresponding author at: Polito[BIO]Med Lab, Department of Mechanical and Aerospace Engineering, Politecnico di Torino, Corso Duca degli Abruzzi 24, 10129 Turin, Italy.
E-mail address: diego.gallo@polito.it (D. Gallo).

https://doi.org/10.1016/j.medengphy.2024.104144
Received 26 September 2023; Received in revised form 5 February 2024; Accepted 9 March 2024
Available online 11 March 2024

Nomenclature

PIV	Particle Image Velocimetry
PTV	Particle Tracking Velocimetry
cw	Continuous Wave
LAD	Left Anterior Descending
CCD	Charge-Coupled Device
CMOS	Complementary Metal-Oxide Semiconductor
IW	Interrogation Window
Re	Reynolds number
RT	Residence Time

recirculation regions [20–25]. These flow features have been linked to relevant biological mechanisms such as fibrin clot formation and growth [22,23,26–28].

Time-resolved PIV-based and PTV-based reconstructions of flow fields can be derived adopting the same experimental setup, usually composed of the three following main elements: a high-speed camera able to perform time-resolved acquisitions, a high-power pulsed laser, and a synchronization unit [17,29,30]. The need for these components poses two main issues hampering the adoption of PIV and PTV in both research and industrial laboratories. The first one is related to the cost of the components. The second issue is related to the safety precautions required for the use of high-power (double-) pulsed lasers, which belong to the most hazardous class in international standards (e.g., IEC 60825-1), and require compliance to strict requirements (e.g., EN 207 in EU; ANSI Z136 in US).

In recent years, attempts have been made to overcome the above-mentioned issues using cameras embedded in commercial smartphones [31–33] or action cameras [34] as image acquisition devices, in some cases in combination with low-power light sources such as continuous wave (*cw*) lasers [31] or LEDs [33,34] to illuminate the fluid domain of interest. These alternative setups were used to perform PIV measurements on relatively simple flow fields, such as the one developing in presence of a jet [31] or a single vortex ring [33]. More recently, we demonstrated the feasibility of PIV measurements in realistic phantoms of healthy and stenotic coronary arteries at various flow regimes adopting a commercial smartphone in combination with a low-power *cw* laser [35], with a tenfold cost reduction with respect to conventional PIV setups.

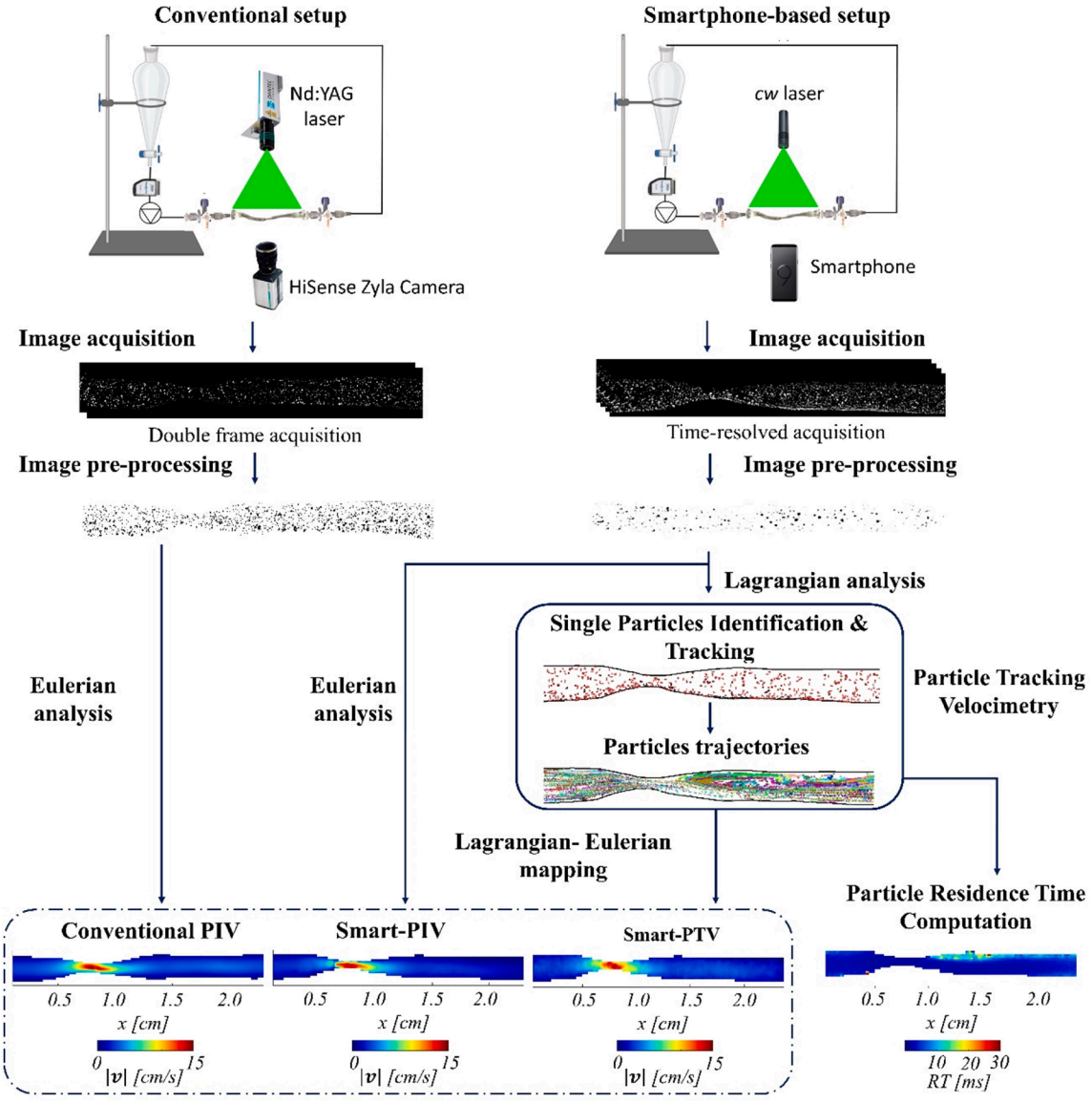

Fig. 1. Workflow adopted for the conventional and smartphone-based acquisitions and processing.

To date, the combined use of smartphone cameras and low-energy light sources has been adopted to obtain only Eulerian representations of the flow field based on PIV measurements, although the Lagrangian description provided by PTV would enrich the Eulerian one in terms of visualization and quantification of flow topology, transport properties, and dynamical path history of particles. Based on these observations, the present study aims to demonstrate the feasibility of low-cost PTV measurements using a smartphone camera and a *cw* laser to characterize the flow developing in realistic physical models of healthy and stenotic coronary arteries. Smartphone-based PTV measurements (termed "smart-PTV" in the following) are mapped to a regular grid to obtain a Eulerian flow field representation and to perform a comparison with previously reported smartphone-based PIV ("smart-PIV") measurements, and with conventional PIV measurements, namely adopting state-of-the-art setup and image processing for the *in vitro* characterization of arterial hemodynamics [35]. The proposed approach potentially lowers the barriers of *in vitro* hemodynamic characterization in terms of costs, safety, ease of use and energy consumption.

2. Materials and methods

A summary of the workflow adopted for the conventional and smartphone-based acquisitions and processing is provided in Fig. 1. Two distinct measurement systems were adopted, a conventional setup for PIV measurements and a smartphone-based setup. The images acquired with the smartphone were analyzed with PIV and PTV techniques to obtain Eulerian and Lagrangian representations of the flow field, respectively. The Lagrangian analysis was based on two steps, namely particle identification and particle tracking. Subsequently, particle Residence Time (*RT*) was assessed, and a Lagrangian–Eulerian mapping was performed to convert the smart-PTV velocity data to Eulerian data on a regular grid. Smart-PIV and smart-PTV Eulerian velocity measurements were compared with those obtained with a conventional PIV system.

2.1. Experimental setups

The two setup configurations presented in Fig. 1 were adopted in this study for smartphone-based PTV and PIV measurements, and for conventional PIV measurements.

Smartphone-based measurements and conventional PIV measurements were performed in two (scale 1:1) flexible silicone phantoms, as described elsewhere [35]. One phantom reproduced the geometry of a patient-specific healthy left anterior descending (LAD) coronary artery, reconstructed from angiographic images [36]. The other phantom was obtained by artificially generating a 67% diameter stenosis in the healthy LAD geometry. The two phantoms were manufactured by Elastrat (Geneva, Switzerland). The refractive index of the material adopted for the phantoms was equal to 1.43.

PIV and PTV velocity measurements were carried out under steady-state flow condition at different flow regimes in both phantoms. Table 1 summarizes the performed experiments, including the Reynolds numbers at the inflow section (Re_{inflow}) and the corresponding flow rate values (Q) for both healthy and stenotic LAD phantoms. The Reynolds numbers in correspondence of the stenosis ($Re_{stenosis}$) are also reported for the stenotic LAD phantom (Table 1). A wide range of flow rate values is investigated to define the range of applicability of smart-PTV measurements. A 500 ml of mixture composed of 60% distilled water and 40% glycerol by volume was used as working fluid, handled by a direct current pump (RS Components, Corby, United Kingdom). Flow rate measurements were obtained by an in-line ultrasound flowmeter (Transonic, Ithaca, USA) characterized by an accuracy of ±10% (Fig. 1). The working fluid was seeded with polyamide particles (density 1030 kg/m^3, diameter 60 μm).

In the smartphone-based setup, a Samsung Galaxy S9+ was adopted as imaging system. It was hold on a tripod at ∼ 10 cm away from the phantom. The acquisition frame rate f of the smartphone in the so-called "super-slow-motion" modality was $f = 960$ Hz, with 1280×720 pixels resolution and f-stop of the objective $f_\# = 2.4$. In smartphone-based measurements, image pairs were acquired at a fixed time interval of 1042 μs (Table 1), corresponding to an image acquisition frame rate of 960 Hz.

Table 1
Investigated flow regimes for the healthy and stenotic LAD phantoms under steady-state condition. Re_{inflow} Reynolds number at the inflow section; $Re_{stenosis}$ Reynolds number at the stenosis section; Q inlet flow rate; Δt interframe time interval adopted for conventional and smartphone-based measurements.

Re_{inflow}	$Re_{stenosis}$	Q [ml/min]	Δt [μs] Conventional PIV setup	Δt [μs] Smartphone-based setup
			Healthy LAD	
43	/	20	1993	1042
85	/	40	997	
171	/	80	498	
213	/	100	400	
			Stenotic LAD	
21	64	10	900	1042
64	192	30	300	
107	320	50	180	
171	512	80	112	

A low-power (30 mW, wavelength $\lambda = 532$ nm) *cw* laser was adopted as light source for illuminating the fluid domain of interest (Fig. 1). The thickness of the light sheet was approximately 1 mm. Due to limited RAM of the smartphone, 20 consecutive acquisitions were recorded per each investigated flow regime. Each acquisition recording consisted of 180 consecutive frames. The maximum particle image displacement, equal to 18 pixels, was reached at the stenosis throat at the highest flow rate regime.

In the conventional PIV setup (Fig. 1), the image capture system (Dantec Dynamics) was composed by a HiSense Zyla camera (CMOS, 2560×2160 pixels, 49 fps single frame in global shutter) with a macro-objective Zeiss Milvus 50 mm ($f_\# = 16$). The light source for the illumination consisted in a dual pulsed Nd:YAG laser (200 mJ, 15 Hz, $\lambda =$ 532 nm) and a synchronization unit. The thickness of the light sheet was set to approximately 1 mm, as for the *cw* laser light sheet in the smartphone-based setup [35]. Image pairs for conventional PIV measurements were acquired at a time interval Δt (Table 1) ensuring a maximum particle image displacement of 10 pixels, as previously suggested [17]. The statistical convergence was assured acquiring 1000 image pairs per each investigated flow regime.

2.2. Image processing and Particle Image Velocimetry measurements

From the raw images acquired in the smartphone-based setup and in the conventional PIV setup, the average intensity value calculated on the raw image sequence per each flow rate was subtracted to reduce background noise and wall reflections. On pre-processed images, the ensemble correlation method [37,38] implemented in the Matlab toolbox PIVlab [39] was applied to extract the velocity vector fields from smartphone images and from images from conventional PIV [35]. In the ensemble correlation method, the correlation matrices from a series of sparsely seeded images from a steady flow experiment were calculated and then averaged to give higher vector field resolution and signal-to-noise ratio than standard PIV algorithms [37]. The obtained velocity fields were further processed for outlier detection and replacement. The outliers were identified and removed by applying the universal outlier detection algorithm based on the local median filter [40] and the velocity vectors associated with the detected outliers were then replaced by interpolation [39]. Interrogation Windows (IWs) of 16×16 pixels with 50% overlap was adopted for conventional PIV, following the recommendation to ensure at least 10 particles per IW

[17]. The IW size for smart-PIV was set to 24×24 pixels with 50% overlap to ensure approximately the same physical dimensions in the object plane of smart-PIV and conventional PIV.

2.3. Particle Tracking Velocimetry (PTV)

2.3.1. Particle Tracking Velocimetry algorithm

The time-resolved acquisitions of the smartphone camera allowed to track individual seeding particles and characterize their motion within the field of view, thus performing smart-PTV measurements. Technically, the adopted PTV algorithm is based on a two-steps strategy: identification of single particles position (step 1); tracking of detected particles over time through the identification of their coordinates in subsequent frames (step 2).

As for step 1, the identification of the position of a single particle in every frame is performed by thresholding the image to remove the background, converting it into a binary image and detecting the centroid of each particle with sub-pixel precision. As for the particle tracking (step 2), the local particle displacement in two consecutive frames is first predicted by exploiting a preliminary smart-PIV measured velocity field $\dot{x}_{PIV}$. In detail, starting from the identified coordinates $(x_{i,t}, y_{i,t})$ of the *i-th* particle centroid at time *t*, the predicted position $(\hat{x}_{i,t+\Delta t}, \hat{y}_{i,t+\Delta t})$ at the subsequent frame acquired at time $t+\Delta t$ is obtained under the hypothesis of uniformly rectilinear motion (Eq. (1)):

$$\begin{cases} \hat{x}_{i,t+\Delta t} = x_{i,t} + \dot{x}_{PIV} \cdot \Delta t \\ \hat{y}_{i,t+\Delta t} = y_{i,t} + \dot{y}_{PIV} \cdot \Delta t \end{cases} \quad (1)$$

where $(\dot{x}_{PIV}, \dot{y}_{PIV})$ are the velocity components resulting from the preliminary smart-PIV analysis at that location. In the predicted position, a circular research area is explored (Fig. 2) with a research radius defined according to the smart-PIV maximum particle displacement for each flow regime [41,42]. Then, within the research area, a nearest-neighbor scheme is implemented to identify the seeding particle located in the nearest position from the predicted one. The identified position is then added to the reconstructed trajectory.

Once the trajectory of the *i-th* particle is reconstructed, the Lagrangian velocity $(\dot{x}_{i,t}, \dot{y}_{i,t})$ and acceleration $(\ddot{x}_{i,t}, \ddot{y}_{i,t})$ can be evaluated by employing a 2D finite difference scheme [17], according to:

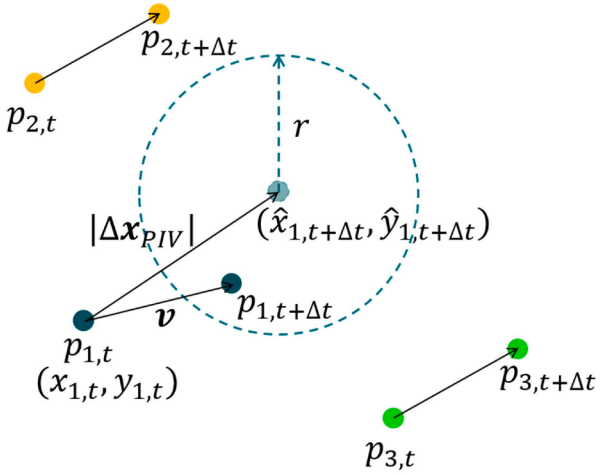

Fig. 2. Particles tracking step in consecutive frames. $p_{1,t}$, $p_{2,t}$ and $p_{3,t}$ particles at time instant *t*; $p_{1,t+\Delta t}$, $p_{2,t+\Delta t}$ and $p_{3,t+\Delta t}$ corresponding particles at time instant $t+\Delta t$; $(x_{1,t}, y_{1,t})$ spatial coordinates of particle 1 at time instant *t*; $(\hat{x}_{1,t+\Delta t}, \hat{y}_{1,t+\Delta t})$ expected spatial coordinates of particle 1 at time instant $t+\Delta t$ computed from PIV results ($|\Delta \boldsymbol{x}_{PIV}| = \sqrt{x_{PIV}^2 + y_{PIV}^2}$); *r* research radius.

$$\begin{cases} \dot{x}_{i,t} = \dfrac{x_{i,t+\Delta t} - x_{i,t-\Delta t}}{2\,\Delta t} \\ \dot{y}_{i,t} = \dfrac{y_{i,t+\Delta t} - y_{i,t+\Delta t}}{2\,\Delta t} \end{cases} \quad (2)$$

$$\begin{cases} \ddot{x}_{i,t} = \dfrac{\dot{x}_{i,t+\Delta t} - \dot{x}_{i,t-\Delta t}}{2\,\Delta t} \\ \ddot{y}_{i,t} = \dfrac{\dot{y}_{i,t+\Delta t} - \dot{y}_{i,t-\Delta t}}{2\,\Delta t} \end{cases} \quad (3)$$

2.3.2. Particle Residence Time quantification

The Residence Time (*RT*) is a trajectory-based indicator of the presence of flow stagnation and recirculation. Adopting the approach proposed in other studies [20,21], *RT* was quantified as the average time spent by particles within a sub-region *R* of 12×12 pixels fixed dimensions:

$$RT = \frac{1}{N_t} \sum_{i=1}^{N_t} RT_i \quad (4)$$

with $RT_i = \Delta t \cdot \sum_{j=1}^{N_T} t_j$ and $\begin{cases} t_j = 1 \text{ if } p_i \in R \\ t_j = 0 \text{ if } p_i \in R \end{cases}$ where N_t is the total number of trajectories crossing the sub-region *R*, RT_i is the residence time of the *i-th* particle, N_T the total number of time steps that the particle p_i spends in the sub-region and t_j is the indicator taking into account the presence of a specific particle p_i within the sub-region *R*. The dimension of the sub-region *R* was determined as a compromise between spatial resolution and number of particles detected within each sub-region. The resulting dimension was 12×12 pixels, thus improving the spatial resolution of *RT* with respect to the Eulerian analysis. By construction, *RT* is expected to be high in the flow separation region distal to a stenosis [20–23]. Consequently, *RT* can be mapped to compare the extension of the recirculation regions forming in the presence of a stenosis at different flow regimes.

2.4. Eulerian mapping of PTV measurements

In the analysis of particle tracking data, ensemble averaging with spatial bins was applied to generate a Eulerian representation of the flow field to perform a quantitative comparison with smart-PIV and conventional PIV measurements. Technically, Lagrangian quantities, characterized by a scattered grid, were mapped into a Eulerian regular grid of size set equal to the IW adopted for smart-PIV measurements (i.e., 16×16 pixels with 50% of overlapping). To obtain the Lagrangian–Eulerian conversion, the velocity vector in the *k-th* IW was obtained by averaging the velocity vectors associated with the particle trajectories going through the *k-th* IW [9,43]. Only trajectories composed by more than six consecutive particle positions were considered. Fig. 3 shows a schematic description of the Eulerian velocity field reconstruction from smart-PTV Lagrangian measurements.

The Eulerian velocity vector fields reconstructed from the smart-PTV Lagrangian data were then post-processed for outlier detection and replacement, applying the same scheme adopted for the PIV data [44]. To complete the analysis, the velocity values obtained from the smartphone-based *vs.* conventional measurements in correspondence of the centerline of the measured flow domain, where velocities are expected to be maximum, were quantitatively compared in terms of average percentage difference ($\bar{\Delta}$) according to:

$$\bar{\Delta} = \frac{1}{N} \sum_{j=1}^{N} \frac{\left| |\boldsymbol{v}|_j^{Smart} - |\boldsymbol{v}|_j^{Conventional} \right|}{|\boldsymbol{v}|_j^{Conventional}} \quad (5)$$

where $|\boldsymbol{v}|_j^{Smart}$ is the smart-PIV or smart-PTV velocity, $|\boldsymbol{v}|_j^{Conventional}$ the velocity magnitude measured with conventional PIV, and *N* is the total number of data points in the considered centerline.

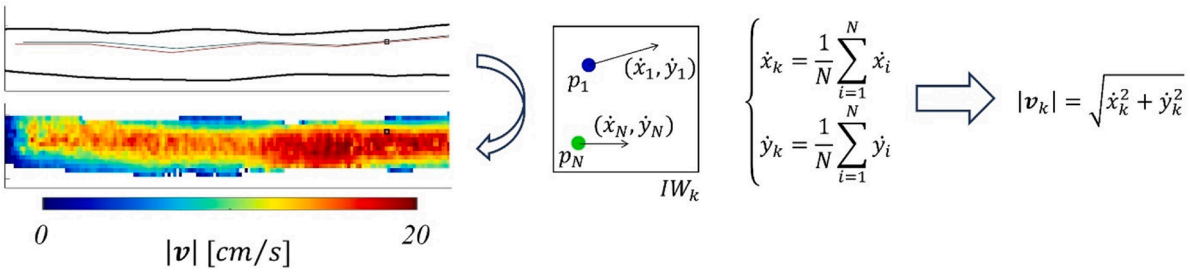

Fig. 3. Schematic description of the Eulerian velocity field reconstruction from Lagrangian information. p_1 and p_N are the particles within the sub-domain IW_k, whose velocity vectors have the components $(\dot{x}_1,\dot{y}_1)$ and $(\dot{x}_N,\dot{y}_N)$, respectively. For the IW_k interrogation window, the velocity components for the Eulerian reconstruction are obtained averaging the velocity components of all the particles found in IW_k. Finally, the velocity magnitude ($|\boldsymbol{v}_k|$) for IW_k is computed.

2.4.1. Vorticity computation

After PIV and PTV analyses, the Eulerian flow fields were further characterized in terms of vorticity [45,46]. In detail, from the performed two components, two-dimensional measurements, the out-of-plane component of the vorticity vector field $\boldsymbol{\omega}_z$, i.e., the vorticity component along the direction orthogonal to the measurement plane, can be calculated (Eq. (6)):

$$\boldsymbol{\omega}_z = \nabla \times \boldsymbol{v} \tag{6}$$

where $\nabla\times\boldsymbol{v}$ is the rotor of the velocity $\boldsymbol{v}$, whose components are $(\dot{x},\dot{y})$.

3. Results

3.1. Particle Tracking Velocimetry

The PTV-based analysis of the flow field detects the location and extension of the recirculation region occurring in the stenotic phantom distal to the stenosis starting from low flow rate regimes ($Re_{inflow} = 64$). As Re_{inflow} increases, the recirculation region stretches axially and grows, as presented in Fig. 4. By visual inspection of the trajectories in the region distal to the stenosis, the motion of recirculation with trajectories characterized by low velocity clearly emerges (Fig. 4). Moreover, smart-PTV measurements also highlight the interaction between the flow recirculation region and the jet flow produced at the throat of the stenosis: it can be noticed that trajectories at the border of the recirculation region undergo a sudden increase of velocity magnitude, as they are captured by the jet flow (Fig. 4). For completeness, the trajectories developing in the healthy phantom, where flow is relatively undisturbed, are reported in the Supplementary Material (Supplementary Figure S1).

3.2. Particle Residence Time computation

Smart-PTV measurements allowed also evaluating the Residence Times in the recirculation region distal to the stenosis region. The *RT* contour maps presented in Fig. 5 clearly show that regions of elevated *RT* values are located near wall distal to the stenosis and extend distally with respect to the recirculation region highlighted by the Lagrangian particle trajectories presented in Fig. 4.

3.3. Eulerian mapping of PTV measurements and comparison with smart-PIV and conventional PIV

The comparison of the contours of the normalized velocity magnitude obtained from conventional PIV, smart-PIV and smart-PTV measurements in the healthy LAD phantom is presented in Fig. 6 at four different flow regimes. Overall, maps of velocity magnitude obtained from smartphone-based measurements are in agreement with conventional PIV measurements. In general, the velocity fields reconstructed from smart-PTV measurements overestimate high velocities less than

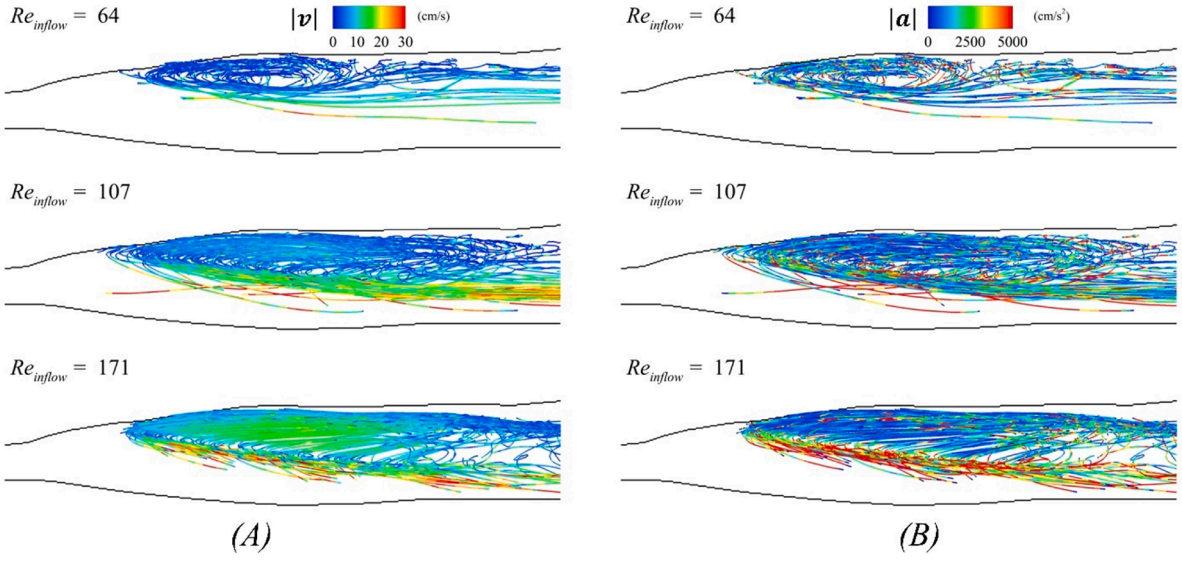

Fig. 4. Stenotic LAD phantom: Lagrangian particle trajectories within the post-stenotic recirculation region at three flow regimes ($Re_{inflow} = 64$, $Re_{inflow} = 107$, $Re_{inflow} = 171$). At $Re_{inflow} = 21$ the recirculation region is not present. Particle trajectories are colored according to the corresponding velocity magnitude (A) and acceleration magnitude (B) values. Only particle trajectories characterized by a change in sign along the path (indicative of retrograde flow) and including more than ten particle positions are displayed. For $Re_{inflow} = 107$ and $Re_{inflow} = 171$ one every five trajectories is displayed.

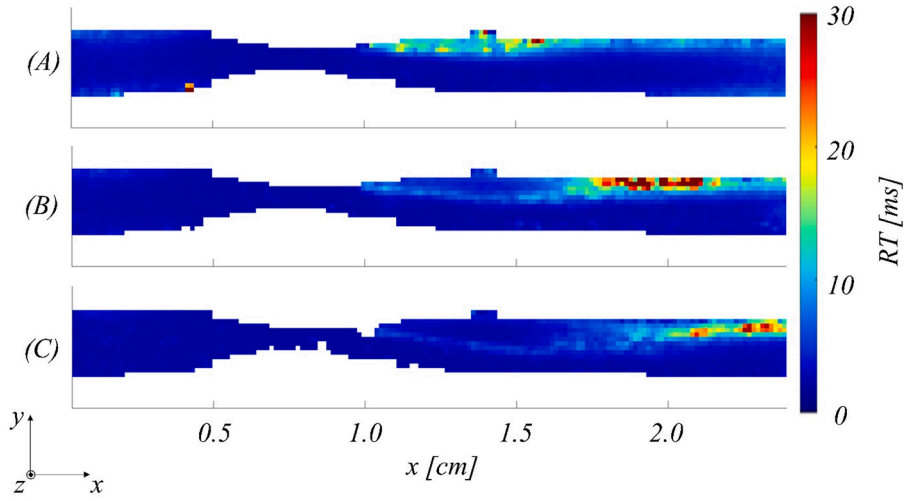

Fig. 5. Stenotic LAD phantom: particle Residence Time (*RT*) evaluated at the post-stenotic region at three different flow regimes ($Re_{inflow} = 64$, $Re_{inflow} = 107$, $Re_{inflow} = 171$).

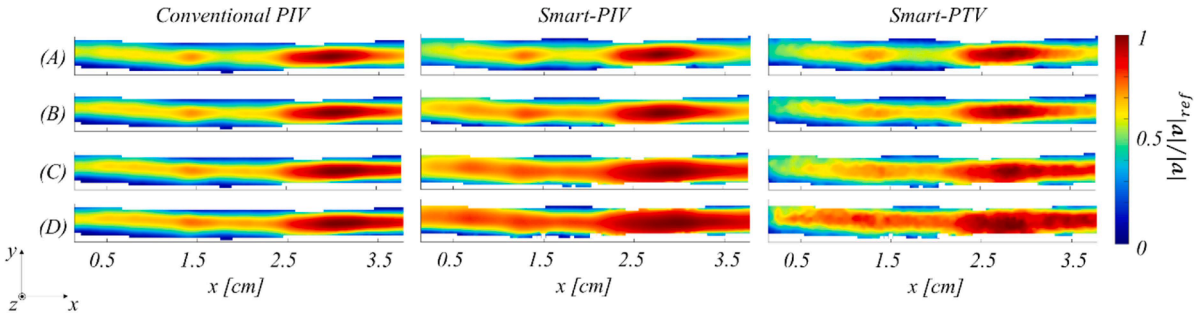

Fig. 6. Healthy LAD phantom: normalized velocity magnitude contours for conventional PIV, smart-PIV and smart-PTV at flow regimes (A) $Re_{inflow} = 43$, (B) $Re_{inflow} = 85$, (C) $Re_{inflow} = 171$, (D) $Re_{inflow} = 213$. The velocity magnitude ($|\boldsymbol{v}|$) is normalized to its maximum value ($|\boldsymbol{v}|_{ref}$). The flow is moving from left to right.

smart-PIV measurements (Fig. 6).

A detailed analysis of the velocity magnitude along the coronary artery phantom length was performed considering the measurements along the centerline of the measured flow domain, where maximum velocities are expected. For the healthy phantom, such an analysis shows that smart-PTV data are in better agreement with conventional PIV than smart-PIV (Fig. 7). Quantitatively, moderate discrepancies with respect to conventional PIV measurements emerge at locations where the velocity magnitude is higher and become more marked as Re_{inflow} increases. At the flow regime with $Re_{inflow} = 43$, the average percentage difference in velocity magnitude from conventional PIV was 4.7 % and 8.0 % when considering smart-PTV-based or smart-PIV measurements, respectively. Such average percentage differences in velocity magnitude increased to 10.5 % and 10.7 % for smart-PTV and smart-PIV, respectively, at the highest flow regime ($Re_{inflow} = 213$, Fig. 7).

The contours of the normalized velocity magnitude obtained from conventional PIV, smart-PIV and smart-PTV measurements in the stenotic LAD phantom at the four different flow regimes are presented in Fig. 8. The two smartphone-based approaches successfully captured the main features in the flow field highlighted by conventional PIV, although some discrepancies with respect to conventional PIV measurements emerge in the post-stenotic jet flow for both smart-PTV-based and smart-PIV measurements (Fig. 8). The velocity magnitude values along the centerline of the measurement plane, shown in Fig. 9, revealed that flow velocity at the throat of the stenosis is underestimated by the smartphone-based setups, with average percentage difference $\bar{\Delta}$ in the range 35.3–49.8 % when considering smart-PIV *vs.* conventional PIV and 28.6–53.1 % when considering smart-PTV *vs.* conventional PIV. As previously reported, such an underestimation in velocity magnitude values with respect to conventional PIV can be ascribed to the particle image blur affecting smartphone-based measurements as the consequence of the combination of high flow velocity with strong velocity gradients, the image acquisition frequency of the smartphone, and the use of a continuous light source [35].

3.4. Vorticity computation

Nondimensional vorticity maps are shown in Fig. 10 for the stenotic LAD phantom only, as vorticity is negligible in the healthy flow fields. The conventional PIV setup captures the increase of the vorticity component ω_z^* in correspondence of the stenosis and its expected increase with the increasing flow regime, in accordance with previous observations [45]. For increasing Re_{inflow}, the presence of decreasing ω_z^* negative values in the post-stenotic region highlight the boundary of the flow separation region, where shear is larger. In smartphone-based measurements, vorticity values are in substantial agreement with the conventional PIV results for the lowest Re_{inflow}, while for higher Re_{inflow}, ω_z^* is underestimated at the stenosis throat and overestimated in the stenosis distal region, compared to conventional PIV. Notably, the boundary of the flow separation region is consistent among the three techniques. The vorticity contour maps for the healthy phantom are reported in the Supplementary Material (Supplementary Figure S2).

4. Discussion

The rapidly advancing and ubiquitous smartphone technology has

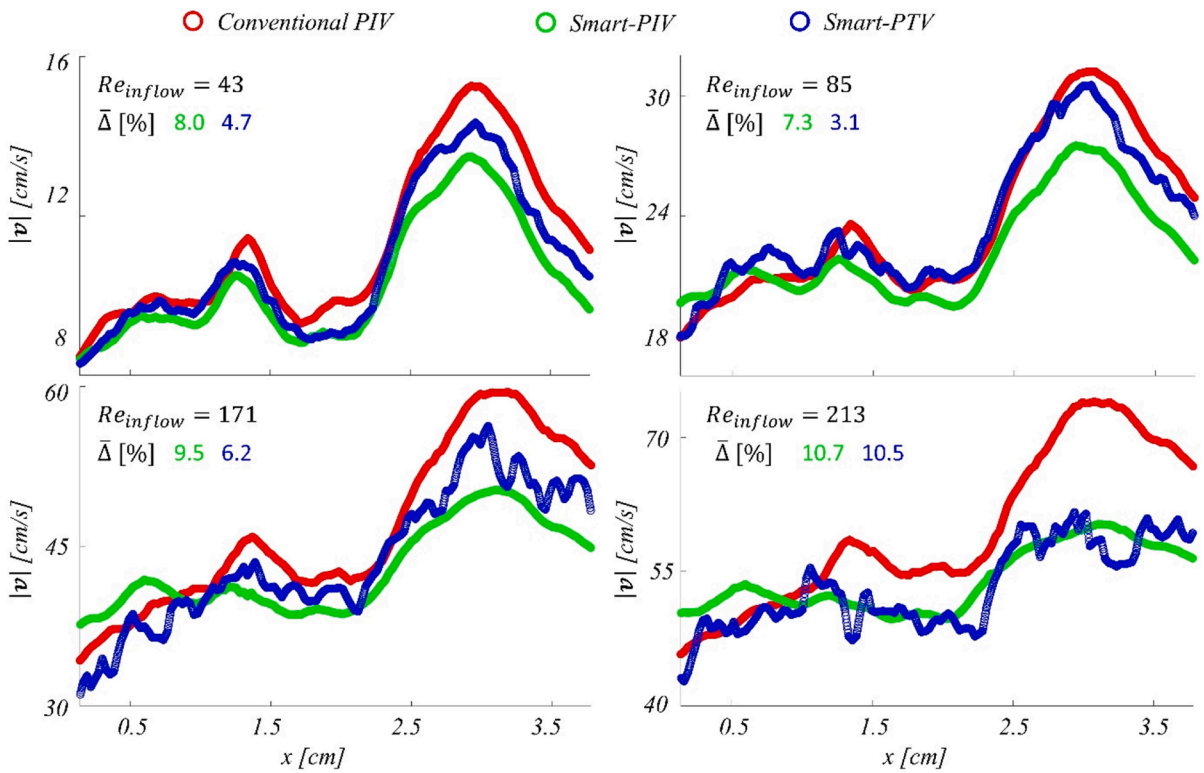

Fig. 7. Healthy LAD phantom: velocity magnitude along the length of the vessel, in correspondence of the centerline of the vessel at the four investigated flow regimes. Average percentage differences ($\bar{\Delta}$) are calculated with respect to conventional PIV and are reported for smart-PIV (green) and smart-PTV (blue).

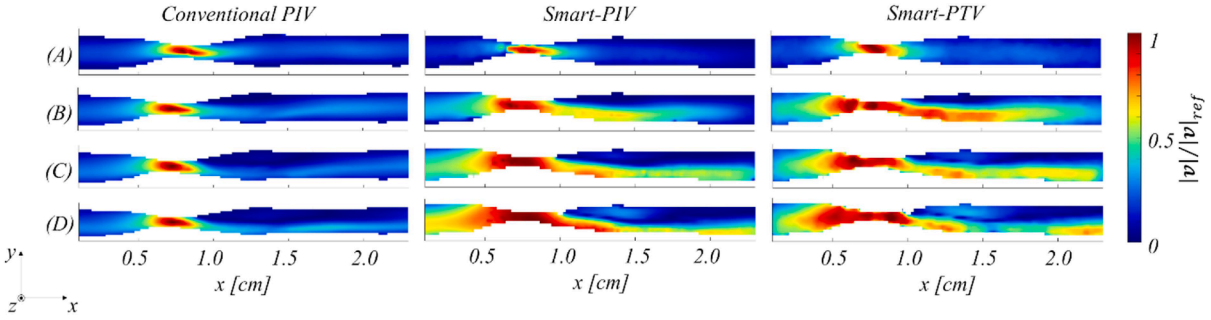

Fig. 8. Stenotic LAD phantom: normalized velocity magnitude contours for conventional PIV, smart-PIV and smart-PTV at flow regimes (A) Re_{inflow} = 21, (B) Re_{inflow} = 64, (C) Re_{inflow} = 107, (D) Re_{inflow} = 171. The velocity magnitude ($|\boldsymbol{v}|$) is normalized to its maximum value ($|\boldsymbol{v}|_{ref}$).

been adopted in very recent years for real-time visualizations and exploration of complex fluid dynamics, with increasing application in various research domains [31–33,35,47]. The use of smartphones brought several advantages in terms of versatility, low-cost, ease of use, operability, and compactness. These advantages are enhanced when combined with the adoption of a low-cost *cw* laser as in this study, where the synchronization between camera and light source is not required and hence costs are further reduced with respect to conventional setups. Additionally, *cw* lasers are markedly cheaper and easier to maintain and operate, less hazardous and use less energy than conventional lasers for anemometric applications. However, no study to date has addressed the feasibility of PTV measurements relying on smartphone cameras and low-energy lasers, as previous studies focused on PIV measurements. The first application adopted a commercial smartphone with an acquisition frequency of 240 Hz and was thus limited to visualizations of flow regimes characterized by moderate flow velocities [31]. Other studies combined the use of smartphones with LEDs as light source, for instance to perform three-dimensional tomographic PIV measurements on a vortex ring employing four smartphones and four pulsed LEDs [33]. Action cameras have been used as well in combination with LEDs to set up relatively low-cost test-benches for stereoscopic PIV measurements of the jet of an aquarium pump [34]. The first application of a smartphone-based PIV setup to study cardiovascular flows was recently proposed to investigate the fluid dynamics in the healthy and stenotic coronary phantoms used in the present study [35]. Qualitative flow visualizations and quantitative 2D velocity vector fields were obtained with the smart-PIV setup and compared to conventional PIV measurements, demonstrating a substantial agreement. Since displacement errors and uncertainties evaluated with the particle disparity method [48] were comparable between smart-PIV and conventional PIV ($\approx$ 5% for the normalized estimated displacement error and below 1.2 pixels for displacement uncertainty), it was concluded that an adequately robust experimental characterization of coronary flows can be obtained with the smart-PIV approach [35]. The present study extends the smart-PIV approach by demonstrating the feasibility of PTV measurements based on the use of a smartphone as image acquisition device and a *cw* laser as

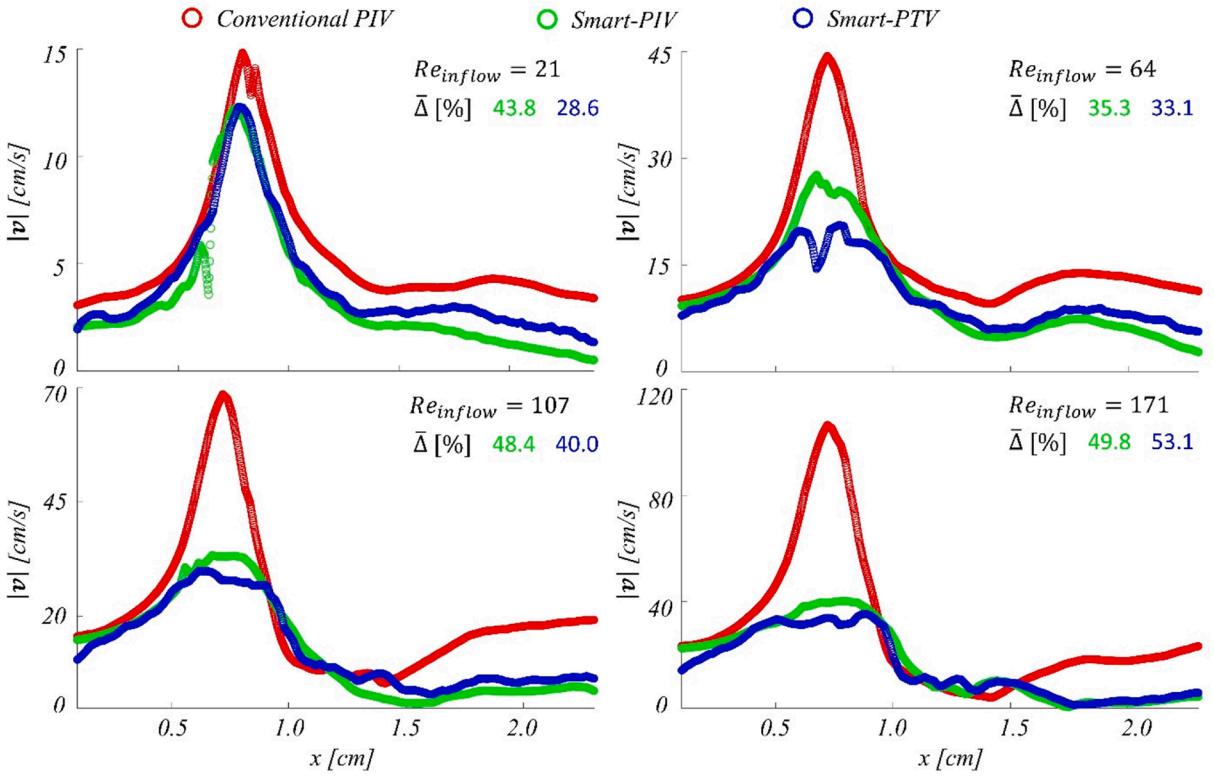

Fig. 9. Stenotic LAD phantom: time-averaged velocity magnitude trends in correspondence of the centerline of the vessel for the four investigated flow regimes. Average percentage differences ($\bar{\Delta}$) are calculated with respect to conventional PIV and are reported for smart-PIV (green) and smart-PTV (blue).

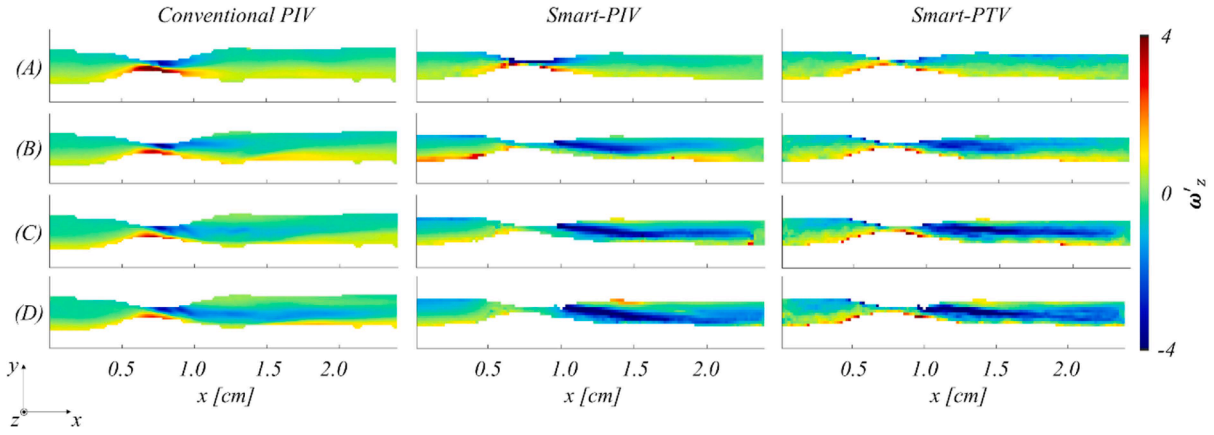

Fig. 10. Stenotic LAD phantom: vorticity contour maps along the z-direction normalized via the inlet diameter d_{inlet} and the maximum velocity magnitude $|\boldsymbol{v}|_{ref}$ $\left(\omega'_z = \boldsymbol{\omega}_z \cdot \frac{d_{inlet}}{|\boldsymbol{v}|_{ref}}\right)$ for conventional PIV, smart-PIV and smart-PTV at flow regimes (A) $Re_{inflow} = 21$, (B) $Re_{inflow} = 64$, (C) $Re_{inflow} = 107$, (D) $Re_{inflow} = 171$.

light source.

The three velocimetry techniques adopted in this study differ in terms of components and processing of the acquired images. The components of the conventional PIV (i.e., CCD camera, high-power dual pulsed laser, and synchronization unit) provide appropriate reference measurements thanks to the acquisition of highly resolved images in both space and time. Conversely, smart-PIV and smart-PTV approaches rely on the same components (i.e., a smartphone and a low-power *cw* laser) but differ in terms of image processing. On one hand, smart-PIV acquired images undergo the same processing workflow as conventional PIV images. On the other hand, smart-PTV is based on the direct knowledge of particle positions to obtain their velocity and acceleration. Previously reported conventional PIV and smart-PIV measurements [35] are used here as a point of reference against which smart-PTV measurements are compared. PTV offers the advantage of evaluating single particle displacement, which is not affected by bias errors resulting from averaging the correlation matrices within the same IW in presence of spatial velocity gradients, as may occur in ensemble correlation PIV measurements [37,49]. Moreover, the here adopted strategy of using *a priori* information to initialize the particle tracking step for the PTV measurements offers the advantage of a smaller research radius in two consecutive frames with respect to traditional PTV algorithms, significantly reducing the number of falsely detected trajectories, with the consequence of increasing the accuracy of the Lagrangian analysis [50]. Additionally, particle image density can be increased overcoming issues of traditional PTV algorithms, otherwise usually requiring low seeding

densities and a particle displacement smaller than the mean spacing between particles [17,29,30,49].

The present study explores for the first time the feasibility of low-cost PTV measurements for the *in vitro* characterization of coronary flows. As main finding, smart-PTV measurements can provide a quantitative Lagrangian characterization of healthy and stenosed coronary hemodynamics, capturing main flow features such as flow recirculation and the associated particle residence times. Moreover, smart-PTV allows obtaining a Eulerian representation of the velocity field characterized by a moderately higher accuracy with respect to the smart-PIV in the healthy LAD phantom, when considering results of the conventional PIV as reference. This is consistent with previous studies, although they were not based on a smartphone setup [49,51]. However, both smartphone-based velocity measurements suffer from an underestimation of the velocities that becomes relevant at the highest investigated flow regime ($Re_{inflow} = 213$, Figs. 6 and 7). Consequently, the observed average percentage differences are lower for the smart-PTV results with respect to the smart-PIV for all the investigated flow regimes and they increase as Re_{inflow} increases, starting from 8 % (smart-PIV) and 4.7 % (smart-PTV) at $Re_{inflow} = 43$ and reaching almost the same value (10.7 % for smart-PIV and 10.5 % for smart-PTV) at $Re_{inflow} = 213$. In the stenotic phantom, the smart-PTV approach captures post-stenotic flow features like flow separation and recirculation (Fig. 8), even though discrepancies emerged with respect to the conventional PIV (Fig. 9), due to the 960 Hz image acquisition frequency of the smartphone camera and the set shutter speed [35]. As expected, the errors computed in the determination of the velocity fields are reflected on ω'_z, leading to its underestimation in the stenotic throat and its overestimation in the post-stenotic region (Fig. 10) for both smart-PIV and smart-PTV with respect to conventional PIV. However, the obtained ω'_z fields highlight an effect of the stenosis in the production of vorticity consistent with previous studies [45]. To complement the Eulerian analysis, we here demonstrate that smart-PTV Lagrangian characterization properly captures the main fluid structures characterizing the stenotic phantom (Fig. 4) [9,21,41,52] enabling the quantitative analysis based on *RT*. Regions of elevated *RT* may indicate the potential for fibrin thrombus formation, as areas of increased *RT* experience stagnant flow where fibrin clot tends to form, grow and potentially embolize resulting in acute ischemia [23,26–28].

The smartphone and *cw* laser-based approach herein proposed for the *in vitro* characterization of the flow in coronary arteries presents limitations that are related to the hardware components, as extensively discussed elsewhere [35]. However, the applicability of the smartphone-based setup can be assessed *a priori* when planning the experiments. In detail, the main limitations of the smartphone-based setup arise from the limited acquisition frame rate and the shutter speed set by default of the smartphone cameras currently available on the market (for the device adopted in this study, 960 Hz), which may cause an underestimation of the higher velocities in the measurements on the stenotic phantom. Moreover, the relatively low shutter speed available at the set acquisition frame rate, combined with the use of a *cw* light source, results in particle image blur in the stenotic throat, where marked flow acceleration occurs [35]. This is reflected in both smart-PIV Eulerian velocity measurements and Lagrangian smart-PTV measurements, as it affects particle centroid determination. To reduce particle blurring, a possibility could be offered by the adoption of a *cw* laser pulsed by a frequency generator [32], or of a pulsed low-power light source such as LEDs [33,34,47] to illuminate the image sensor for a short time. However, these solutions would increase the cost of the setup as they would require a synchronization unit. Another possibility relies on recent advancements in smartphone technology leading to the production of smartphones that record video at a frame rate up to 1920 Hz (e.g., Xiaomi 12 Pro, Huawei Mate 40 Pro). In this sense, it is expected that the next-generation smartphone cameras will enable to measure flow fields characterized by extended ranges of velocity values.

5. Conclusions

This study demonstrates for the first time the feasibility of PTV measurements in the field of cardiovascular flows using a smartphone-based setup, here applied for the *in vitro* characterization of the fluid dynamics in realistic phantoms of healthy and diseased coronary arteries. The proposed setup represents a sustainable, low maintenance, safe and low-cost solution that expands the recently demonstrated feasibility of smart-PIV measurements [35], by obtaining (1) detailed path-dependent quantities highlighting flow separation/recirculation regions characterizing the hemodynamics in stenotic coronary arteries, and (2) Eulerian quantities characterized by higher accuracy with respect to smart-PIV measurements. Although limitations such as the image acquisition frequency and the camera shutter speed currently affect the applicability of smartphone-based measurements, these will be possibly outdone in future technological developments. Thus, it is expected that smartphone-based setups will be increasingly used for research, industrial and educational purposes and to perform reliable preliminary flow investigations at remarkably lower costs than conventional anemometric setups.

Funding

This work has been supported by the Italian Ministry of Education, University and Research (FISR2019_03221, CECOMES). BG scholarship is part of the project PNNR-NGEU, which has received funding from the MUR – DM 352/2022.

Ethical approval

Not required

Declaration of competing interest

None declared

Supplementary materials

Supplementary material associated with this article can be found, in the online version, at doi:10.1016/j.medengphy.2024.104144.

References

[1] Secomb TWHemodynamics. Compr Physiol 2016;6:975–1003. https://doi.org/10.1002/cphy.c150038.
[2] Kwak BR, Bäck M, Bochaton-Piallat ML, Caligiuri G, Daemen MJAP, Davies PF, et al. Biomechanical factors in atherosclerosis: mechanisms and clinical implications. Eur Heart J 2014;35:3013–20. https://doi.org/10.1093/eurheartj/ehu353.
[3] Morbiducci U, Kok AM, Kwak BR, Stone PH, Steinman DA, Wentzel JJ. Atherosclerosis at arterial bifurcations: evidence for the role of haemodynamics and geometry. Thromb Haemost 2016;115:484–92. https://doi.org/10.1160/th15-07-0597.
[4] Trigui A, Ben Chiekh M, Béra JC, Gilles B. Experimental and numerical investigation of pulsed flows in asevere aortic stenosed model. Med Eng Phys 2021;90:33–42. https://doi.org/10.1016/j.medengphy.2021.02.006.
[5] Alam N, Walsh M, Newport D. Experimental evaluation of a patient specific Brachio-Cephalic Arterio Venous Fistula (AVF): velocity flow conditions under steady and pulsatile waveforms. Med Eng Phys 2022;106:103834. https://doi.org/10.1016/j.medengphy.2022.103834.
[6] Zhang Y, Zhang R, Thomas N, Ullah AH, Eichholz B, Estevadeordal J, et al. Experimental and computational study of pulsatile flow characteristics in Romanesque and gothic aortic arch models. Med Eng Phys 2022;102:103784. https://doi.org/10.1016/j.medengphy.2022.103784.
[7] Yazdi SG, Geoghegan PH, Docherty PD, Jermy M, Khanafer A. A review of arterial phantom fabrication methods for flow measurement using PIV techniques. Ann Biomed Eng 2018;46:1697–721. https://doi.org/10.1007/s10439-018-2085-8.
[8] Scardulla F, Bellavia D, D'Acquisto L, Raffa GM, Pasta S. Particle image velocimetry study of the celiac trunk hemodynamic induced by continuous-flow left ventricular assist device. Med Eng Phys 2017;47:47–54. https://doi.org/10.1016/j.medengphy.2017.06.029.

[9] Gülan U, Lüthi B, Holzner M, Liberzon A, Tsinober A, Kinzelbach W. Experimental study of aortic flow in the ascending aorta via particle tracking velocimetry. Exp Fluids 2012;53:1469–85. https://doi.org/10.1007/s00348-012-1371-8.

[10] Brunette J, Mongrain R, Laurier J, Galaz R, Tardif JC. 3D flow study in a mildly stenotic coronary artery phantom using a whole volume PIV method. Med Eng Phys 2008;30:1193–200. https://doi.org/10.1016/j.medengphy.2008.02.012.

[11] Lim WL, Chew YT, Chew TC, Low HT. Steady flow dynamics of prosthetic aortic heart valves. J Biomech 1998;31:411–21. https://doi.org/10.1016/S0021-9290(98)00026-8.

[12] Charonko J, Karri S, Schmieg J, Prabhu S, Vlachos P. In vitro, time-resolved PIV comparison of the effect of stent design on wall shear stress. Ann Biomed Eng 2009;37:1310–21. https://doi.org/10.1007/s10439-009-9697-y.

[13] Li Q, Hegner F, Bruecker CH. Comparative study of wall-shear stress at the ascending aorta for different mechanical heart valve prostheses. J Biomech Eng 2020;142:011006. https://doi.org/10.1115/1.4043357.

[14] Tomaszewski M, Sybilski K, Baranowski P, Małachowski J. Experimental and numerical flow analysis through arteries with stent using particle image velocimetry and computational fluid dynamics method. Biocybern Biomed Eng 2020;40:740–51. https://doi.org/10.1016/j.bbe.2020.02.010.

[15] Gülan U, Appa H, Corso P, Templin C, Bezuidenhout D, Zilla P, et al. Performance analysis of the transcatheter aortic valve implantation on blood flow hemodynamics: an optical imaging-based in vitro study. Artif Organs 2019;43:E282–93. https://doi.org/10.1111/aor.13504.

[16] Brindise MC, Chiastra C, Burzotta F, Migliavacca F, Vlachos PP. Hemodynamics of stent implantation procedures in coronary bifurcations: an in vitro study. Ann Biomed Eng 2017;45:542–53. https://doi.org/10.1007/s10439-016-1699-y.

[17] Raffel M, Willert CE, Scarano F, Kähler CJ, Wereley ST, Kompenhans J. Particle image velocimetry. Cham: Springer International Publishing; 2018. p. 1–283. https://doi.org/10.1007/978-3-319-68852-7.

[18] Qureshi MH, Tien W-H, Lin Y-JP. Performance comparison of particle tracking velocimetry (PTV) and particle image velocimetry (PIV) with long-exposure particle streaks. Meas Sci Technol 2021;32:2. https://doi.org/10.1088/1361-6501/abb747.

[19] Kähler CJ, Scharnowski S, Cierpka C. On the uncertainty of digital PIV and PTV near walls. Exp Fluids 2012;52:1641–56. https://doi.org/10.1007/s00348-012-1307-3.

[20] Tsao R, Jones SA, Giddens DP, Zarins CK, Glagov S. Measurement of particle residence time and particle acceleration in an arterial model by an automatic particle-tracking system. Proceedings of the SPIE 1993;1801:744–53. https://doi.org/10.1117/12.145832.

[21] Balducci A, Grigioni M, Querzoli G, Romano GP, Daniele C, D'Avenio G, et al. Investigation of the flow field downstream of an artificial heart valve by means of PIV and PTV. Exp Fluids 2004;36:204–13. https://doi.org/10.1007/s00348-003-0744-4.

[22] Raz S, Einav S, Alemu Y, Bluestein D. DPIV prediction of flow induced platelet activation—comparison to numerical predictions. Ann Biomed Eng 2007;35:493–504. https://doi.org/10.1007/s10439-007-9257-2.

[23] Jeronimo MD, Zhang K, Rival DE. Direct Lagrangian measurements of particle residence time. Exp Fluids 2019;60:72. https://doi.org/10.1007/s00348-019-2718-1.

[24] Jeronimo MD, Rival DE. Particle residence time in pulsatile post-stenotic flow. Phys Fluids 2020;32:045110. https://doi.org/10.1063/1.5144388.

[25] Steinman DA. Simulated pathline visualization of computed periodic blood flow patterns. J Biomech 2000;33:623–8. https://doi.org/10.1016/S0021-9290(99)00205-5.

[26] Long CC, Esmaily-Moghadam M, Marsden AL, Bazilevs Y. Computation of residence time in the simulation of pulsatile ventricular assist devices. Comput Mech 2014;54:911–9. https://doi.org/10.1007/s00466-013-0931-y.

[27] Reininger AJ, Reininger CB, Heinzmann U, Wurzinger LJ. Residence time in niches of stagnant flow determines fibrin clot formation in an arterial branching model - detailed flow analysis and experimental results. Thromb Haemost 1995;74:916–22. https://doi.org/10.1055/s-0038-1649847.

[28] Tambasco M, Steinman DA. Path-dependent hemodynamics of the stenosed carotid bifurcation. Ann Biomed Eng 2003;31:1054–65. https://doi.org/10.1114/1.1603257.

[29] Adrian R. Particle-imaging techniques for experimental fluid mechanics. Annu Rev Fluid Mech 1991;23:261–304. https://doi.org/10.1146/annurev.fluid.23.1.261.

[30] Tropea C, Yarin AL, Foss JF. Springer handbook of experimental fluid mechanics. Berlin. Heidelberg: Springer Berlin Heidelberg; 2007. p. 215–446. https://doi.org/10.1007/978-3-540-30299-5.

[31] Cierpka C, Hain R, Buchmann NA. Flow visualization by mobile phone cameras. Exp Fluids 2016;57:108. https://doi.org/10.1007/s00348-016-2192-y.

[32] Cierpka C, Otto H, Poll C, Hüther J, Jeschke S, Mäder P. SmartPIV: flow velocity estimates by smartphones for education and field studies. Exp Fluids 2021;62:172. https://doi.org/10.1007/s00348-021-03262-z.

[33] Aguirre-Pablo AA, Alarfaj MK, Li EQ, Hernández-Sánchez JF, Thoroddsen ST. Tomographic particle image velocimetry using smartphones and colored shadows. Sci Rep 2017;7:3714. https://doi.org/10.1038/s41598-017-03722-9.

[34] Käufer T, König J, Cierpka C. Stereoscopic PIV measurements using low-cost action cameras. Exp Fluids 2021;62:57. https://doi.org/10.1007/s00348-020-03110-6.

[35] Caridi GCA, Torta E, Mazzi V, Chiastra C, Audenino AL, Morbiducci U, et al. Smartphone-based particle image velocimetry for cardiovascular flows applications: a focus on coronary arteries. Front Bioeng Biotechnol 2022;10:1011806. https://doi.org/10.3389/fbioe.2022.1011806.

[36] Lodi Rizzini M, Gallo D, De Nisco G, D'Ascenzo F, Chiastra C, Bocchino PP, et al. Does the inflow velocity profile influence physiologically relevant flow patterns in computational hemodynamic models of left anterior descending coronary artery? Med Eng Phys 2020;82:58–69. https://doi.org/10.1016/j.medengphy.2020.07.001.

[37] Santiago JG, Beebe DJ, Wereley ST, Meinhart CD, Adrian RJ. A particle image velocimetry system for microfluidics. Exp Fluids, 25; 1998. p. 316–9. https://doi.org/10.1007/s003480050235.

[38] Meinhart CD, Wereley ST, Santiago JG. A PIV algorithm for estimating time-averaged velocity fields. J Fluids Eng 2000;122:285–9. https://doi.org/10.1115/1.483256.

[39] Thielicke W, Stamhuis EJ. PIVlab – towards user-friendly, affordable and accurate digital particle image velocimetry in MATLAB. J Open Res Softw 2014;2(1):e30. https://doi.org/10.5334/jors.bl.

[40] Westerweel J. Efficient detection of spurious vectors in particle image velocimetry data. Exp Fluids 1994;16:236–47. https://doi.org/10.1007/BF00206543.

[41] Maas HG, Gruen A, Papantoniou D. Particle tracking velocimetry in three-dimensional flows - part 1. Photogrammetric determination of particle coordinates. Exp Fluids 1993;15:133–46. https://doi.org/10.1007/BF00190953.

[42] Malik NA, Dracos T, Papantoniou DA. Particle tracking velocimetry in three-dimensional flows - part II: Particle tracking. Exp Fluids 1993;15:279–94. https://doi.org/10.1007/BF00223406.

[43] Agüera N, Cafiero G, Astarita T, Discetti S. Ensemble 3D PTV for high resolution turbulent statistics. Meas Sci Technol 2016;27:124011. https://doi.org/10.1088/0957-0233/27/12/124011.

[44] Westerweel J, Scarano F. Universal outlier detection for PIV data. Exp Fluids 2005;39:1096–100. https://doi.org/10.1007/s00348-005-0016-6.

[45] Chu M, von Birgelen C, Li Y, Westra J, Yang J, Holm NR, et al. Quantification of disturbed coronary flow by disturbed vorticity index and relation with fractional flow reserve. Atherosclerosis 2018;273:136–44. https://doi.org/10.1016/j.atherosclerosis.2018.02.023.

[46] Wu JZ, Ma HY, Zhou MD. Vorticity and vortex dynamics. Berlin: Springer; 2006.

[47] Minichiello A, Armijo D, Mukherjee S, Caldwell L, Kulyukin V, Truscott T, et al. Developing a mobile application-based particle image velocimetry tool for enhanced teaching and learning in fluid mechanics: a design-based research approach. Comput Appl Eng Educ 2021;29:517–37. https://doi.org/10.1002/cae.22290.

[48] Sciacchitano A, Wieneke B, Scarano F. PIV uncertainty quantification by image matching. Meas Sci Technol 2013;24:045302. https://doi.org/10.1088/0957-0233/24/4/045302.

[49] Kähler CJ, Scharnowski S, Cierpka C. On the resolution limit of digital particle image velocimetry. Exp Fluids 2012;52:1629–39. https://doi.org/10.1007/s00348-012-1280-x.

[50] Keane RD, Adrian RJ, Zhang Y. Super-resolution particle imaging velocimetry. Meas Sci Technol 1995;6:754. https://doi.org/10.1088/0957-0233/6/6/013.

[51] Janke T, Schwarze R, Bauer K. PIV-PTV comparison of the oscillating flow inside the human lungs. 13th International Symposium on Particle Image Velocimetry – ISPIV 2019; 232-238.

[52] Virant M, Dracos T. 3D PTV and its application on Lagrangian motion. Meas Sci Technol 1997;8:1539–52. https://doi.org/10.1088/0957-0233/8/12/017.